



Contents lists available at SciVerse ScienceDirect

Combustion and Flame

journal homepage: www.elsevier.com/locate/combustflame

Feature Article

Thermodynamic modeling based on a generalized cubic equation of state for kerosene/LOx rocket combustion

Seong-Ku Kim^a, Hwan-Seok Choi^a, Yongmo Kim^{b,*}^aSpace Propulsion Division, Korea Aerospace Research Institute, Daejeon 305-333, Republic of Korea^bDepartment of Mechanical Engineering, Hanyang University, Seoul 133-791, Republic of Korea

ARTICLE INFO

Article history:

Received 26 April 2011

Received in revised form 31 August 2011

Accepted 10 October 2011

Available online xxxx

Keywords:

Generalized cubic equation of state

Kerosene surrogate

Cryogenic oxygen

Thermodynamic non-ideality

Liquid rocket combustion

Flamelet equations

ABSTRACT

Based on a generalized cubic equation of state proposed by Cismonti and Møllerup [Fluid Phase Equilib. 232 (2005) 74–89], this study derived formulations for the thermodynamic properties of mixtures that are needed for combustion simulations of liquid rocket engines. The present model was validated thoroughly against reference data provided by NIST in order to assess its validity over a wide range of critical compressibility factors, pressures, and temperatures. The numerical results clearly indicate that the present model is superior in its handling of fluid mixtures with quite different critical compressibility factors, while maintaining the advantages of the cubic equation of state compared to those of the Soave–Redlich–Kwong and Peng–Robinson equations of state. In addition, steady flamelet analysis has been performed to investigate the effects of detailed chemical kinetics, real fluid behavior, and increased pressure on the local flame structures of the kerosene surrogate and liquid oxygen relevant to liquid rocket engines.

© 2011 The Combustion Institute. Published by Elsevier Inc. All rights reserved.

1. Introduction

Kerosene fuels have been widely used for aviation jet and rocket engines [1]. In the case of rocket applications, the bi-propellant combination of liquid hydrogen (LH₂) and liquid oxygen (LOx) yields a 30% higher specific impulse compared to that of the kerosene and LOx combination. However, the low density of LH₂ leads to a larger tank volume, heavier vehicle mass, and higher aerodynamic drag. Alternatively, because kerosene has a density that is approximately 10 times that of LH₂, the kerosene and LOx propellant combination is competitive, especially for first-stage or booster high-thrust engines, even at the expense of performance. Moreover, non-cryogenic kerosene provides the additional merits of a low operating cost, ease of handling, and no insulation requirement for the fuel tank compared to the cryogenic properties of LH₂.

According to the recent trends in liquid propellant rocket technologies, the chamber pressure has been progressively elevated in order to comply with the practical demands for performance improvement and compactness of the thrust chamber [2]. Since the nozzle expansion ratio at the flow separation point is increased by elevating the chamber pressure, design limitations associated with flow separation can be considerably relaxed. As listed in Table 1, representative engines operate at a combustion chamber

pressure greater than 6 MPa, which is higher than the critical pressures of kerosene (typically 2.3 MPa) and oxygen (5.04 MPa). Therefore, a fundamental understanding of the essential physics underlying high pressure mixing and combustion processes is needed for the reliable design and analysis of these combustion devices in order to meet conflicting requirements in terms of performance, combustion stability, and heat transfer characteristics. However, detailed measurements based on laser diagnostics are quite difficult, mainly due to soot formed by high-order hydrocarbon combustion, as well as the severe environment of the combustion chamber under high pressure (from 6 MPa up to 25 MPa) and high adiabatic flame temperatures exceeding 3500 K. In this respect, it is quite desirable to develop comprehensive models for the numerical simulation of liquid propellant combustion processes at a supercritical pressure. The simulations of the mixing and combustion processes near or above the critical pressure are very challenging problems because of non-ideality in thermodynamics and abnormality of transport properties, in addition to conventional closure problems including turbulence and turbulence-chemistry interactions.

During the last two decades, many experimental and numerical studies have been performed on the issues associated with high pressure mixing and combustion phenomena. In the previous decade, research efforts had been made focusing on the physics of fluid behaviors of single droplet and mixing layers in the supercritical pressure regime, which were critically reviewed by Bellan [3] and Yang [4]. Since then, experimental works have been carried

* Corresponding author. Fax: +82 2 2297 0339.

E-mail address: ymkim@hanyang.ac.kr (Y. Kim).

Table 1
Representative engines of kerosene/LOx propellant rockets [2].

Engine	SLV ^a (stage)	P_{ch} ^b	Engine cycle	Isp_v ^c	Developer (period)
RD-180	Atlas (1st)	25.66	SC ^d	338	Energomash (1992–1998)
RD-120	Zenit (2nd)	16.28	SC	350	Energomash (1976–1985)
RD-0124	Soyuz-2 (3rd)	15.50	SC	359	CADB (1996–1999)
RD-0110	Soyuz (3rd)	6.80	GG ^e	326	CADB (1963–1967)
F-1	Saturn-V (1st)	6.77	GG	305	Rocketdyne (1959–1967)
RD-107	Soyuz (1st)	5.88	GG	313	Energomash (1954–1957)

^a Space launch vehicle.

^b Combustion chamber pressure (unit: MPa).

^c Specific impulse at vacuum (unit: s).

^d Staged combustion.

^e Gas-generator.

out on more realistic problems such as the high-pressure injection of cryogenic nitrogen and GH_2/LOx coaxial shear injectors, and the achievements by advanced research groups have been compiled in Ref. [5]. Such work has recently progressed to include practical studies of the single-injector or multiple-injectors of a sub-scale combustion chamber with propellant combinations of GH_2/LOx or GCH_4/LOx . A series of experiments clearly indicates that cryogenic liquid jets injected at a supercritical pressure have no clear inter-phase boundary. Thus, at supercritical conditions, subcritical spray combustion processes accompanying liquid atomization, droplet breakup, droplet-turbulent interactions, and vaporization no longer occur. The supercritical combustion of cryogenic liquid propellants is predominantly controlled by turbulent diffusion and is characterized by extremely high density gradients and real fluid behaviors. According to the experimental findings, recent numerical studies on liquid rocket combustion at supercritical pressures are conceptually based on a single-phase mixture model of general fluids, accounting for thermodynamic non-ideality and anomalous transport properties. This model is distinctly different from the conventional two-phase model which separately treats the subcritical cascade processes such as atomization, droplet breakup, droplet vaporization, turbulent mixing, and chemical reactions. Ribert et al. [6] suggested a comprehensive model for studying laminar counterflow diffusion flames of hydrogen and oxygen over subcritical, transcritical, and supercritical states. Their model incorporates a unified treatment of general fluid thermodynamics [7] into an existing flow solver so as to address detailed chemical kinetics and multispecies transport. The numerical method was extended by Pons et al. to numerically analyze the effects of pressure and strain rate on the transcritical mass transfer and combustion in the nonpremixed counterflow flames of methane and oxygen [8]. Utilizing the library obtained with the counterflow diffusion flame model [6,8], there has been an ongoing research effort [9] to develop an advanced real-fluid turbulent combustion model in the framework of the laminar flamelet model. Similarly, Cutrone et al. [10] have recently modified a flamelet-reaction-progress-variable approach based on the single-phase real-fluid mixture model to generate the flamelet library for RANS simulation, which was validated against several test cases including cryogenic nitrogen injection, GH_2/LOx , and GCH_4/LOx coaxial flames at supercritical pressures. Their numerical results demonstrated that the real fluid effects strongly affect the mixing and flame fields near the injectors.

Although several sophisticated EoS exist such as the BWR (Benedict-Webb-Rubin) model, they have scarcely been applied to multi-component reacting flow calculations due to complex nonlinear forms and computational inefficiency. Therefore, in order to describe the thermodynamic properties of real fluids, most of the numerical studies [6–11] have so far relied on the two-parameter cubic EoS such as the Soave–Redlich–Kwong (SRK) [12] and Peng–Robinson (PR) [13,14] models because of the compromise

between engineering accuracy and ease of implementation. Recently, Cismondi and Mollerup [15] have proposed a generalized cubic EoS with three parameters to overcome the intrinsic limitations of the two-parameter cubic EoS. However, this newly developed EoS [15] has only been used to calculate density behavior and global phase equilibrium in mixtures and has not yet been applied to other engineering applications.

The primary objective of this work is to develop the thermodynamic model based on the three-parameter cubic EoS to simulate mixing and combustion of liquid propellants at high pressures. For this goal, the three-parameter cubic EoS has been extended to a mixture composed of an arbitrary number of components with the conventional mixing rule, and all of the thermodynamic properties needed for the calculation of reacting flows have been derived in detail from fundamental thermodynamic theories. Validations of the present thermodynamic models have been made against the NIST database [16,17] for cryogenic oxygen and a three-component surrogate mixture of kerosene, as well as the Burke–Schumann flame sheet of oxygen and the kerosene surrogate over a wide range of pressures and temperatures. Next, steady flamelet analysis based on the present thermodynamic modeling has been performed to numerically investigate the nonpremixed flame structures of kerosene and LOx subject to supercritical pressures. Based on the numerical results, detailed discussions are made for the essential features of the local flame structures of kerosene and LOx in the supercritical pressure conditions encountered in a liquid propellant rocket engine.

2. Mathematical formulations

2.1. Generalized cubic equation of state

The widely used cubic equations of state can be commonly expressed in the following equation with two model constants u and w [14].

$$p = \frac{\rho R_u T}{M_w - b\rho} - \frac{a\alpha(T)\rho^2}{M_w^2 + uM_w b\rho + wb^2\rho^2} \quad (1)$$

For the SRK (Soave–Redlich–Kwong) and PR (Peng–Robinson) EoS, u and w become the integer pair of (1,0) and (2, −1), respectively. Parameters a and b take into account the effects of attractive and repulsive forces among molecules, respectively, and are determined by critical temperature and critical pressure. In order to account for the polarity of the species, a is multiplied by a correction factor α which is a function of reduced temperature and an acentric factor. The detailed definitions of the parameters are given in Table 2. Consequently, the cubic Eq. (1) involves the two parameters $a\alpha$ and b to be modeled for a pure fluid or mixture of interest. Recently, Cismondi and Mollerup [15] have pointed out that the limited accuracy of the two-parameter cubic EoS is caused by the inconsistency

Table 2

Parameters of the three cubic equations of state.

Parameter	SRK[12]	PR[13,14]	RK-PR[15]
u	1	2	$\delta_1 + \delta_2$
w	0	-1	$\delta_1 \delta_2$
δ_1	1	$1 + \sqrt{2}$	$d_1 + d_2(d_3 - 1.168Z_c)^{d_4} + d_5(d_3 - 1.168Z_c)^{d_5}$
δ_2	0	$1 - \sqrt{2}$	$\frac{1-\delta_1}{1+\delta_1}$
a	$0.42747 \left(\frac{R_u T_c}{p_c} \right)$	$0.45724 \left(\frac{R_u T_c}{p_c} \right)$	$\frac{3y^2 + 3yd + d^2 + d - 1}{(3y + d - 1)^2} \left(\frac{R_u T_c}{p_c} \right)$
b	$0.08664 \left(\frac{R_u T_c}{p_c} \right)$	$0.07780 \left(\frac{R_u T_c}{p_c} \right)$	$\frac{1}{3y + d - 1} \left(\frac{R_u T_c}{p_c} \right)$
			where $d = (1 + \delta_1^2)/(1 + \delta_1)$, $y = 1 + [2(1 + \delta_1)]^{\frac{1}{3}} + \left(\frac{4}{1 + \delta_1} \right)^{\frac{1}{3}}$
α	$\left[1 + S \left(1 - \sqrt{T/T_c} \right) \right]^2$ where $S = 0.48508$ $+1.55171\omega$ $-0.15613\omega^2$	$\left[1 + S \left(1 - \sqrt{T/T_c} \right) \right]^2$ where $S = 0.37464$ $+1.54226\omega$ $-0.26992\omega^2$	$\left(\frac{3}{2 + T/T_c} \right)^k$ where $k = (1.168Z_c A_1 + A_0)\omega^2$ $+ (1.168Z_c B_1 + B_0)\omega$ $+ (1.168Z_c C_1 + C_0)$
$\frac{dz}{dT}$		$-\frac{S}{\sqrt{T_c}} \left[1 + S \left(1 - \sqrt{\frac{T}{T_c}} \right) \right]$	$-\frac{3^k k}{T_c (2 + T/T_c)^{k+1}}$
$\frac{d^2 z}{dT^2}$		$\frac{S^2}{2T_c} + \frac{S}{2\sqrt{T_c}} \left[1 + S \left(1 - \sqrt{\frac{T}{T_c}} \right) \right]$	$\frac{3^k k(k+1)}{T_c^2 (2 + T/T_c)^{k+2}}$

in the density dependence of its equation rather than the empirical nature of model constants αx and b . Furthermore, in order to overcome the intrinsic limitations of the two-parameter cubic EoS, they have proposed a three-parameter cubic EoS (hereafter RK-PR EoS) by introducing an additional parameter, δ_1 . In their work, Eq. (1) is expressed in the generalized form

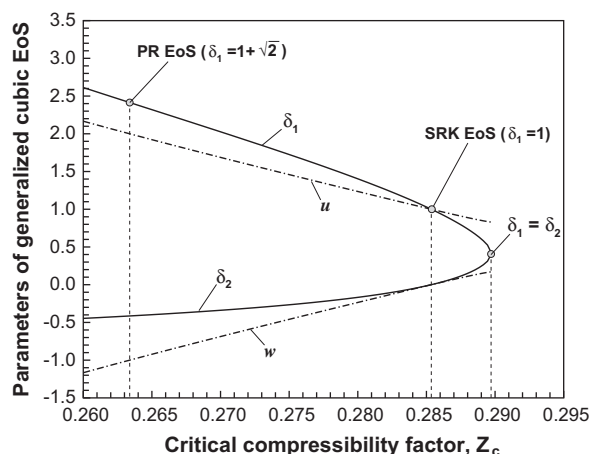
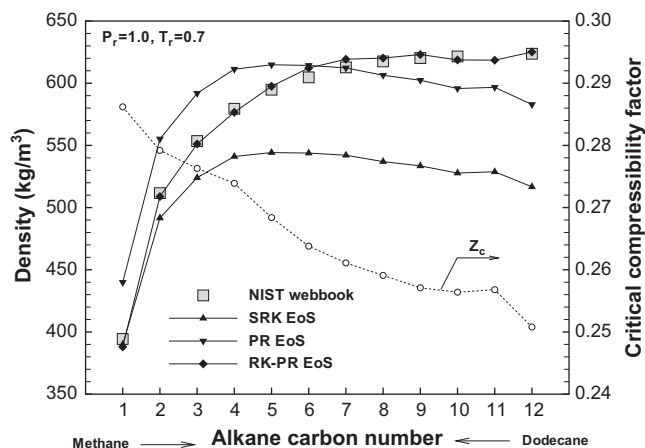
$$p = \frac{\rho R_u T}{M_w - b\rho} - \frac{\alpha x(T) \rho^2}{(M_w + \delta_1 b\rho)(M_w + \delta_2 b\rho)} \quad (2)$$

where δ_2 is a subsidiary parameter and is defined as $(1 - \delta_1)/(1 + \delta_1)$. As summarized in Tables 2 and 3, the third parameter δ_1 of the RK-PR EoS is determined by the critical compressibility factor of fluid (Z_c), and parameters αx and b are subsequently modified by δ_1 . The dependency of the model parameters (δ_1, δ_2, u , and w) on Z_c is graphically illustrated in Fig. 1. If δ_1 is equal to one, Eq. (2) becomes identical to that of the SRK EoS ($u = 1, w = 0$). On the other hand, when δ_1 is $1 + \sqrt{2}$, Eq. (2) reduces to the same form as the PR EoS ($u = 2, w = -1$). This implies that the SRK and PR EoS are special cases of the RK-PR EoS with a specific value of Z_c .

In Fig. 2, the densities of saturated hydrocarbons with varying carbon number, from methane (CH_4) to dodecane ($\text{C}_{12}\text{H}_{26}$), are predicted at the critical pressure and reduced temperature ($T_r = T/T_c$) of 0.7 for each species by the three different cubic EoS and compared with the reference data taken from the NIST webbook [16]. For the two-parameter EoS, the predicted results indicate that the SRK EoS is able to more correctly capture the pVT behaviors of the small molecules having a high Z_c , for example, methane ($Z_c = 0.2862$), whereas the PR EoS seems relatively suitable for the higher hydrocarbons with a lower Z_c , especially heptane with $Z_c = 0.2611$. The RK-PR EoS demonstrates the superior predictive capability over those of the SRK and PR EoS for the whole range

Table 3Model constants for δ_1 and k of the RK-PR EoS [15].

δ_1		k	
d_1	0.428363	A_1	-2.4407
d_2	18.496215	A_0	0.0017
d_3	0.338426	B_1	7.4513
d_4	0.660000	B_0	1.9681
d_5	789.723105	C_1	12.5040
d_6	2.512392	C_0	-2.7238

**Fig. 1.** Dependence of the generalized cubic EoS on the critical compressibility factor.**Fig. 2.** Density versus alkane carbon number calculated by the three different cubic EoS at $p_r = 1.0$ and $T_r = 0.7$.

of critical compressibility factors according to the relationship shown in Fig. 1. The results predicted by the three different cubic EoS conform well to the work of Cismondi and Mollerup [15].

2.2. Extension to a multi-component mixture

In order to extend the RK-PR EoS to a mixture composed of an arbitrary number of components, in this study, the mixture is regarded as a unique pure hypothetical fluid whose parameters required in Eq. (2) are obtained through conventional mixing rules [14].

$$a\alpha = \sum_{i=1}^N \sum_{j=1}^N X_i X_j a_{ij} \alpha_{ij} \quad (3)$$

$$b = \sum_{i=1}^N X_i b_i \quad (4)$$

$$\delta_1 = \sum_{i=1}^N X_i \delta_{1,i} \quad \text{and} \quad \delta_2 = \sum_{i=1}^N X_i \delta_{2,i} \quad (5)$$

where X_i is the mole fraction of individual species i . The first and second derivatives of $a\alpha$ with respect to temperature, which are used for the derivation of the thermodynamic properties in the next subsection, are expressed consistently with the mixing rule of Eq. (3) as follows.

$$\frac{\partial a\alpha}{\partial T} = \sum_{i=1}^N \sum_{j=1}^N X_i X_j \frac{\partial a_{ij} \alpha_{ij}}{\partial T} \quad (6)$$

$$\frac{\partial^2 a\alpha}{\partial T^2} = \sum_{i=1}^N \sum_{j=1}^N X_i X_j \frac{\partial^2 a_{ij} \alpha_{ij}}{\partial T^2} \quad (7)$$

Subsequently, coefficient $a_{ij} \alpha_{ij}$ needs to be determined from the appropriate combination rules. In the present study, two different approaches are considered according to previous works [7,11]. Without any other remarks, the numerical results obtained in this study are based on the second combination rule (CR2).

2.2.1. Combination rule 1 (CR1)

Yang and his colleagues have used the following combination rule for $a_{ij} \alpha_{ij}$ in Eq. (3) in a series of numerical studies [9,18,19] to simulate high pressure vaporization, mixing, and combustion processes in liquid fuel propulsion systems in the context of a unified treatment of general fluid thermodynamics based on the SRK EoS [7].

$$a_{ij} \alpha_{ij} = \sqrt{a_i a_j \alpha_i \alpha_j} (1 - \bar{\kappa}_{ij}) \quad (8)$$

where $\bar{\kappa}_{ij}$ is an empirical parameter of binary interaction. The first and second derivatives of coefficient $a_{ij} \alpha_{ij}$ with respect to the temperature, which appear in Eqs. (6) and (7), can be obtained by differentiating Eq. (8) as follows.

$$\frac{\partial a_{ij} \alpha_{ij}}{\partial T} = \sqrt{a_i a_j} \frac{\partial \sqrt{\alpha_i \alpha_j}}{\partial T} = \sqrt{a_i a_j} \left(\frac{1}{2} \sqrt{\frac{\alpha_i}{\alpha_j}} \frac{\partial \alpha_j}{\partial T} + \frac{1}{2} \sqrt{\frac{\alpha_j}{\alpha_i}} \frac{\partial \alpha_i}{\partial T} \right) \quad (9)$$

$$\begin{aligned} \frac{\partial^2 a_{ij} \alpha_{ij}}{\partial T^2} &= \sqrt{a_i a_j} \frac{\partial^2 \sqrt{\alpha_i \alpha_j}}{\partial T^2} = \sqrt{a_i a_j} \left[\frac{1}{2 \sqrt{\alpha_i \alpha_j}} \frac{\partial \alpha_i}{\partial T} \frac{\partial \alpha_j}{\partial T} \right. \\ &\quad \left. - \frac{1}{4} \sqrt{\frac{\alpha_i}{\alpha_j^3}} \left(\frac{\partial \alpha_j}{\partial T} \right)^2 - \frac{1}{4} \sqrt{\frac{\alpha_j}{\alpha_i^3}} \left(\frac{\partial \alpha_i}{\partial T} \right)^2 + \frac{1}{2} \sqrt{\frac{\alpha_i}{\alpha_j}} \frac{\partial^2 \alpha_j}{\partial T^2} + \frac{1}{2} \sqrt{\frac{\alpha_j}{\alpha_i}} \frac{\partial^2 \alpha_i}{\partial T^2} \right] \end{aligned} \quad (10)$$

Here, the coefficients and derivatives for an individual species (i.e., $a_i, \alpha_i, b_i, \delta_{1,i}, \delta_{2,i}, \partial \alpha_i / \partial T, \partial^2 \alpha_i / \partial T^2$) are given as functions of its critical data and reduced temperature in Table 2.

2.2.2. Combination rule 2 (CR2)

On the other hand, an alternative combination rule formed by introducing the following pseudo-critical parameters was employed in the direct numerical simulations of the supercritical heptane-nitrogen mixing layers by Miller et al. [11].

$$T_{c,ij} = \sqrt{T_{c,i} T_{c,j} (1 - \kappa_{ij})}, \quad p_{c,ij} = Z_{c,ij} (R_u T_{c,ij} / v_{c,ij}), \quad \omega_{ij} = \frac{1}{2} (\omega_i + \omega_j) \quad (11)$$

with

$$v_{c,ij} = \frac{1}{8} \left[v_{c,i}^{1/3} + v_{c,j}^{1/3} \right]^3, \quad Z_{c,ij} = \frac{1}{2} (Z_{c,i} + Z_{c,j}) \quad (12)$$

Subsequently, the off-diagonal $a_{ij} \alpha_{ij}$ can be directly calculated by the same expression used for the diagonals, which is given in Table 2, along with the pseudo-critical parameters in Eq. (11). In this combination rule, the temperature derivatives required in Eqs. (6) and (7) are obtained simply as follows.

$$\frac{\partial a_{ij} \alpha_{ij}}{\partial T} = a_{ij} \frac{\partial \alpha_{ij}}{\partial T} \quad (13)$$

$$\frac{\partial^2 a_{ij} \alpha_{ij}}{\partial T^2} = a_{ij} \frac{\partial^2 \alpha_{ij}}{\partial T^2} \quad (14)$$

Here, $\partial \alpha_{ij} / \partial T$ and $\partial^2 \alpha_{ij} / \partial T^2$ can be calculated by the relations given in Table 2, with the pseudo-parameters $T_{c,ij}$, ω_{ij} , and $Z_{c,ij}$ of Eqs. (11) and (12).

The interaction parameters $\bar{\kappa}_{ij}$ and κ_{ij} which appear in Eqs. (8) and (11), respectively, are related to each other based on their compatibility as second virial coefficients [14]. These empirical parameters are determined experimentally and are known for very limited combinations of the binary mixture [14]. In the present study, therefore, all of the values of the interaction parameters are assumed to be zero.

2.3. Thermodynamic properties based on generalized cubic EOS

Cismondi and Mollerup [15] developed the three-parameter cubic EoS of Eq. (2) mainly to calculate the density behavior and global phase equilibrium in mixtures. However, the newly developed EoS has not yet been applied to other engineering applications. As the first attempt to apply it for numerical simulation of high-pressure mixing and combustion processes, the present study systematically derived all of the thermodynamic properties associated with the multi-component reacting flows based on the generalized cubic EoS and the mixing rule expressed in Eqs. (2)–(5). The detailed procedures are very similar to those in Meng and Yang's work [7], in which the thermodynamic properties and numerical Jacobian matrices are derived based on the SRK EoS from fundamental thermodynamic theories and the concepts of partial-mass and partial-density properties. It is worthwhile to note that, when the value of δ_1 is fixed to unity in all of the formulations for the thermodynamic properties derived in this study, we can obtain identical expressions to those in Meng and Yang's work [7]. Furthermore, the generalized formulations can be straightforwardly applied to the construction of the preconditioning scheme by which Yang and his colleagues have effectively simulated dynamic behaviors of a LO_x droplet within a supercritical hydrogen stream [18] and the turbulent flame of LO_x and GCH₄ mixing layer [9].

By differentiating Eq. (2) with respect to the temperature and densities of the mixture and individual species, respectively, we can obtain the following differential expressions which are used repeatedly in the derivation of thermodynamic properties as well as numerical Jacobian matrices.

$$\left(\frac{\partial p}{\partial T}\right)_{\rho_j} = \frac{\rho R_u}{M_w - b\rho} - \left(\frac{\partial \alpha}{\partial T}\right) \frac{\rho^2}{(M_w + \delta_1 b\rho)(M_w + \delta_2 b\rho)} \quad (15)$$

$$\left(\frac{\partial p}{\partial \rho}\right)_{T,Y_j} = \frac{M_w R_u T}{(M_w - b\rho)^2} - \frac{\alpha \rho M_w [2M_w + (\delta_1 + \delta_2)b\rho]}{(M_w + \delta_1 b\rho)^2 (M_w + \delta_2 b\rho)^2} \quad (16)$$

$$\begin{aligned} \left(\frac{\partial p}{\partial \rho_i}\right)_{T,\rho_{j \neq i}} &= \frac{M_w R_u T}{M_{w,i}(M_w - b\rho)^2} [M_w + \rho(b_i - b)] \\ &\quad - \frac{2\rho M_w \sum_j X_j a_{ij} \alpha_{ij}}{M_{w,i}(M_w + \delta_1 b\rho)(M_w + \delta_2 b\rho)} \\ &\quad + \frac{\alpha \rho^2 M_w b_i}{M_{w,i}(M_w + \delta_1 b\rho)^2 (M_w + \delta_2 b\rho)^2} [(\delta_1 + \delta_2)M_w \\ &\quad + 2\delta_1 \delta_2 b\rho] \end{aligned} \quad (17)$$

By substituting Eqs. (2) and (15) into the fundamental thermodynamic relation for internal energy, the following expression is derived in terms of the reference low-pressure properties and a dense fluid correction.

$$\begin{aligned} e(T, \rho) &= e_0(T) + \int_{\rho_0}^{\rho} \left[\frac{p}{\rho^2} - \frac{T}{\rho^2} \left(\frac{\partial p}{\partial T}\right)_{\rho} \right] d\rho \\ &= e_0(T) + \frac{1}{(\delta_1 - \delta_2)bM_w} \left[T \left(\frac{\partial \alpha}{\partial T}\right) - \alpha \right] \ln \left(\frac{M_w + \delta_1 b\rho}{M_w + \delta_2 b\rho} \right) \end{aligned} \quad (18)$$

Here, subscript 0 refers to the ideal state near atmospheric pressure. In this study, the thermodynamic properties at the ideal state are determined by the Chemkin-II package [20]. To facilitate numerical treatment, the concept of the partial-density property is employed according to the previous work [7]. By multiplying Eq. (18) by the mixture density and differentiating with respect to the density of species i , we obtain the following equation for the partial-density internal energy of species i .

$$\begin{aligned} \tilde{e}_i &= \left(\frac{\partial p e}{\partial \rho_i}\right)_{T,\rho_{j \neq i}} = e_{i,0} + \frac{2 \sum_j X_j \left[T \left(\frac{\partial a_{ij} \alpha_{ij}}{\partial T}\right) - a_{ij} \alpha_{ij} \right]}{(\delta_1 - \delta_2)bM_{w,i}} \ln \left(\frac{M_w + \delta_1 b\rho}{M_w + \delta_2 b\rho} \right) \\ &\quad + \frac{b_i \left[T \left(\frac{\partial \alpha}{\partial T}\right) - \alpha \right]}{(\delta_1 - \delta_2)bM_{w,i}} \left[\frac{(\delta_1 - \delta_2)\rho M_w}{(M_w + \delta_1 b\rho)(M_w + \delta_2 b\rho)} - \frac{1}{b} \ln \left(\frac{M_w + \delta_1 b\rho}{M_w + \delta_2 b\rho} \right) \right] \end{aligned} \quad (19)$$

The partial-mass enthalpy of species i is obtained through a relation with the partial-density internal energy of species [7] as follows.

$$h_i = \tilde{e}_i - \frac{\left(\sum_{j=1}^N Y_j \tilde{e}_j - e - \frac{p}{\rho} \right)}{\left(\frac{\partial p}{\partial \rho}\right)_{T,Y_j}} \left(\frac{\partial p}{\partial \rho_i}\right)_{T,\rho_{j \neq i}} \quad (20)$$

where the two derivatives of pressure are given by Eqs. (16) and (17). Now, the specific enthalpy of the mixture is obtained by the definition.

$$h = \sum_{i=1}^N Y_i h_i \quad (21)$$

The specific heat capacity at constant-volume is determined by differentiating Eq. (18) with respect to temperature.

$$c_v = \left(\frac{\partial e}{\partial T}\right)_{\rho,Y_j} = c_{v,0} + \frac{T}{(\delta_1 - \delta_2)bM_w} \left(\frac{\partial^2 \alpha}{\partial T^2}\right) \ln \left(\frac{M_w + \delta_1 b\rho}{M_w + \delta_2 b\rho} \right) \quad (22)$$

The constant-pressure specific heat and speed of sound can be obtained using the fundamental thermodynamic relationship [7] as follows.

$$c_p = c_v + \frac{T}{\rho^2} \frac{\left(\frac{\partial p}{\partial T}\right)_{\rho_j}^2}{\left(\frac{\partial p}{\partial \rho}\right)_{T,Y_j}} \quad (23)$$

$$c^2 = \left(\frac{\partial p}{\partial \rho}\right)_{s,Y_j} = \frac{c_p}{c_v} \left(\frac{\partial p}{\partial \rho}\right)_{T,Y_j} \quad (24)$$

Similar to the specific internal energy, the following expression for specific entropy is derived.

$$\begin{aligned} s(T, \rho) &= s_0(T, \rho_0) - \int_{\rho_0}^{\rho} \left[\frac{1}{\rho^2} \left(\frac{\partial p}{\partial T}\right)_{\rho} \right] d\rho \\ &= s_0(T, \rho_0) + \frac{R_u}{M_w} \ln \left(1 - \frac{b\rho}{M_w} \right) - \frac{R_u}{M_w} \ln \left(\frac{\rho}{\rho_0} \right) \\ &\quad + \left(\frac{\partial \alpha}{\partial T}\right) \frac{1}{(\delta_1 - \delta_2)bM_w} \ln \left(\frac{M_w + \delta_1 b\rho}{M_w + \delta_2 b\rho} \right) \end{aligned} \quad (25)$$

The ideal gas entropy is defined using the standard-state at atmospheric pressure as a reference.

$$s_0(T, \rho_0) = \sum_{i=1}^N \left[\int_{T_{ref}}^T \frac{c_{p,i,0}}{T} dT + s_{i,0}(T_{ref}) - \frac{R_u}{M_{w,i}} \ln X_i - \frac{R_u}{M_{w,i}} \ln \left(\frac{p}{p_{atm}} \right) \right] Y_i \quad (26)$$

Differentiating the product of Eq. (25) and the mixture density with respect to the density of species i leads to the following formulation for the partial-density entropy of species i .

$$\begin{aligned} \tilde{s}_i &= \left(\frac{\partial \rho s}{\partial \rho_i}\right)_{T,\rho_{j \neq i}} \\ &= \int_{T_{ref}}^T \frac{c_{p,i,0}}{T} dT + s_{i,0}(T_{ref}) - \frac{R_u}{M_{w,i}} (1 + \ln X_i) - \frac{R_u}{M_{w,i}} \\ &\quad \times \ln \left(\frac{\rho R_u T / M_w}{p_{atm}} \right) + \frac{R_u}{M_{w,i}} \ln \left(1 - \frac{b\rho}{M_w} \right) - \frac{R_u b_i}{M_{w,i}} \frac{\rho}{(M_w - b\rho)} \\ &\quad + \frac{2 \sum_j X_j \left(\frac{\partial a_{ij} \alpha_{ij}}{\partial T}\right)}{(\delta_1 - \delta_2)bM_{w,i}} \ln \left(\frac{M_w + \delta_1 b\rho}{M_w + \delta_2 b\rho} \right) \\ &\quad + \frac{b_i \left(\frac{\partial \alpha}{\partial T}\right)}{(\delta_1 - \delta_2)b^2 M_{w,i}} \left[\frac{(\delta_1 - \delta_2)b\rho M_w}{(M_w + \delta_1 b\rho)(M_w + \delta_2 b\rho)} - \ln \left(\frac{M_w + \delta_1 b\rho}{M_w + \delta_2 b\rho} \right) \right] \end{aligned} \quad (27)$$

Lastly, the partial-mass specific entropy of species i can be obtained through the fundamental thermodynamic relation.

$$s_i = \tilde{s}_i + \frac{1}{\rho} \frac{\left(\frac{\partial p}{\partial T}\right)_{\rho_j}}{\left(\frac{\partial p}{\partial \rho}\right)_{T,Y_j}} \left(\frac{\partial p}{\partial \rho_i}\right)_{T,\rho_{j \neq i}} \quad (28)$$

In summary, the three cubic EoS (SRK, PR, RK-PR) are commonly expressed in the generalized equation of Eq. (2), although the parameters are calculated differently for each EoS. The density can be obtained non-iteratively by solving the cubic polynomial equation with a given temperature, pressure, and species concentration. Furthermore, the thermodynamic properties are derived through the fundamental thermodynamic relations with the generalized cubic equation and its derivatives. The computational costs for each of the three different cubic EoS are almost the same because additional computing time due to the third parameter δ_1 is negligible.

2.4. Flamelet equations

The local flame structures embedded in the turbulent flame field can be effectively described by the flamelet equations which account for the non-equilibrium effects caused by competition between the chemical kinetics and molecular diffusion processes enhanced by turbulent mixing [21]. With the unitary Lewis-number

assumption for all participating chemical species, the flamelet equations are expressed with respect to the mixture fraction Z as follows.

$$\frac{\partial Y_i}{\partial t} = \frac{\chi}{2} \frac{\partial^2 Y_i}{\partial Z^2} + \dot{\omega}_i \quad (29)$$

$$\frac{\partial T}{\partial t} = \frac{\chi}{2} \left[\frac{\partial^2 T}{\partial Z^2} + \frac{1}{c_p} \frac{\partial c_p}{\partial Z} \frac{\partial T}{\partial Z} + \frac{\partial T}{\partial Z} \sum_{k=1}^N \left(1 - \frac{c_{pk}}{c_p} \right) \frac{\partial Y_k}{\partial Z} \right] - \frac{1}{\rho c_p} \sum_{k=1}^N h_k \dot{\omega}_k \quad (30)$$

The constant-pressure specific heat changes drastically with a sharp peak when the real fluid mixture undergoes the transcritical transition at the pseudo-boiling points. Therefore, instead of the conventional form of the flamelet energy equation of Eq. (30), we use the equivalent energy equation [22], which replaces derivatives of the temperature and constant-pressure specific heat with the second derivative of enthalpy with respect to the mixture fraction as follows.

$$\frac{\partial T}{\partial t} = \frac{\chi}{2} \frac{1}{c_p} \frac{\partial^2 h}{\partial Z^2} - \frac{\chi}{2} \frac{1}{c_p} \sum_{k=1}^N h_k \frac{\partial^2 Y_k}{\partial Z^2} - \frac{1}{\rho c_p} \sum_{k=1}^N h_k \dot{\omega}_k \quad (31)$$

The scalar dissipation rate χ representing the non-equilibrium effects is modeled by the following one-parametric distribution [21].

$$\chi(Z) = \chi_{st} \exp[2(\operatorname{erfc}^{-1}(2Z_{st}))^2 - 2(\operatorname{erfc}^{-1}(2Z))^2] \quad (32)$$

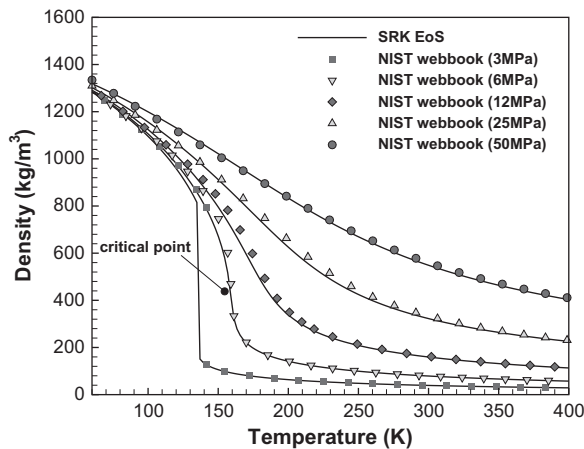
where erfc^{-1} is the inverse of the complementary error function. In general, the stoichiometric scalar dissipation rate χ_{st} describes the departure from the chemical equilibrium. If the stoichiometric scalar dissipation rate in a steady laminar flame exceeds the critical value χ_q , the flame will be quenched.

In this study, the flamelet equations in the mixture fraction space are extended to account for the real fluid behaviors in trans-critical and supercritical states. The real-fluid flamelet code is written utilizing a specific set of subroutines in the Chemkin-II package [20], which is modified to compute the thermodynamic and transport properties of the real fluid mixtures at all thermodynamic states, as mentioned in the previous subsections. For calculation of the steady state solutions for flamelet Eqs. (29) and (31), the two point boundary value problem solver TWOPNT [23] is used.

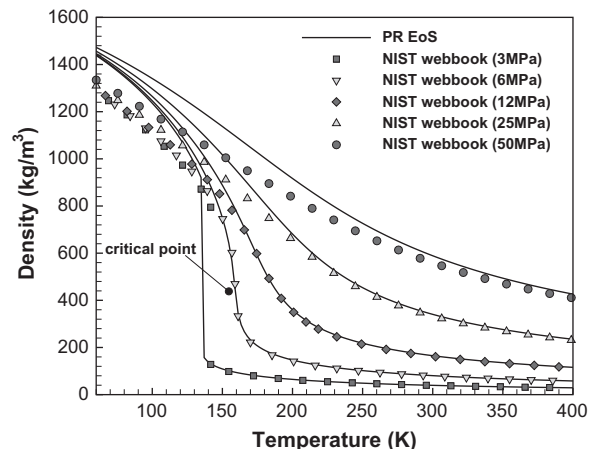
3. Results and discussion

3.1. Thermodynamic properties of oxygen and a kerosene surrogate

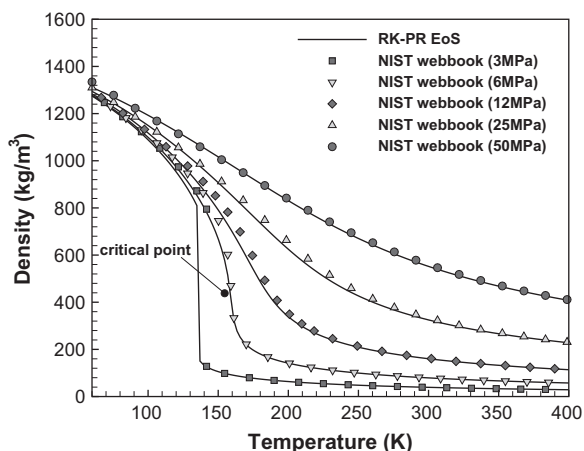
In order to evaluate the accuracy and applicability of the present thermodynamic models, the thermodynamic properties such as density, constant-pressure specific heat, specific enthalpy, entropy, and speed of sound have been calculated for oxygen and a three-component kerosene surrogate over a wide range of operating pressures relevant to the kerosene/LOx rocket engines shown in Table 1.



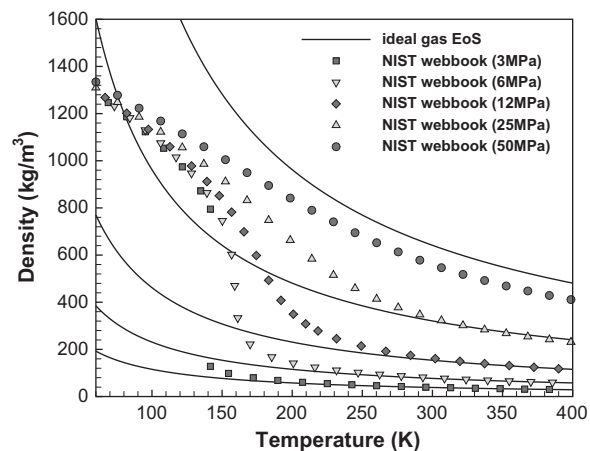
(a) Soave-Redlich-Kwong EoS



(b) Peng-Robinson EoS



(c) Generalized RK-PR EoS



(d) Ideal gas EoS

Fig. 3. Oxygen density versus temperature for five pressures; comparison between the NIST data (webbook) and prediction by four different EoS.

For validation of the pure fluid, the reference data is taken from the NIST webbook [16]. In terms of the oxygen density profiles versus temperature for five pressures, Fig. 3 presents a comparison between the NIST data and results obtained by the three different cubic equations of state (SRK, PR, and RK-PR EoS), as well as by the ideal gas assumption. In comparison with the NIST data, the PR EoS overestimates the densities in the temperature conditions lower than the pseudo-boiling point, whereas the SRK and RK-PR EoS correctly predict the density variation of the cryogenic liquid oxygen over all of the ranges under consideration. Since oxygen has a high critical compressibility factor of 0.2864, the nearly equivalent performances of the SRK and RK-PR EoS can be explained according to the characteristics illustrated in Fig. 1, and the relatively poor capability of the PR EoS is in line with the predictive trend displayed in Fig. 2. As the fluid is heated to a sufficiently high temperature where the real fluid effects become negligible, the density profiles predicted by all real-fluid equations of state approach those of the ideal gas model.

Figure 4 exhibits a comparison between the NIST webbook data and the thermodynamic properties of oxygen predicted by the formulations derived based on the RK-PR EoS. As shown in Fig. 4, the present model yields good agreements with the NIST data for other important thermodynamic properties, such as constant-pressure specific heat, specific enthalpy, entropy, and sound speed over the whole pressure range. The computed results clearly indicate

that the present model predicts a distinctly different evolution of the thermodynamic properties versus temperature compared to that of the ideal gas model. At 6 MPa, which is quite close to the critical pressure of oxygen, the thermodynamic properties are very sensitive to temperature variation. In the temperature range from 130 K to 170 K, the oxygen density drastically decreases, and the constant-pressure specific heat rapidly increases, before sharply decreasing. Especially at 159 K, where the constant-pressure specific heat reaches a peak level, a large amount of heat can be stored without a noticeable increase in temperature, and volume expansion occurs. In the transcritical fluid, this phenomenon is a well-known pseudo-boiling behavior. The enthalpy and entropy are also sensitively varied in the corresponding temperature range. As the pressure increases further, the pseudo-boiling point where the fluid changes from a liquid to a supercritical state, moves toward a higher temperature, and a smoother transition of the thermodynamic properties occurs. At supercritical pressures, as shown in Fig. 4d, the sound speed profiles for the wide pressure and temperature ranges exhibit the essential characteristics of liquid and supercritical fluid for lower and higher temperature regions, respectively, which might be important for the numerical modeling of fluid flow over its entire thermodynamic states.

In terms of the relative errors of the density and constant-pressure specific heat compared to the reference data of the NIST webbook [16], the predictions of the three different cubic EoS (SRK, PR,

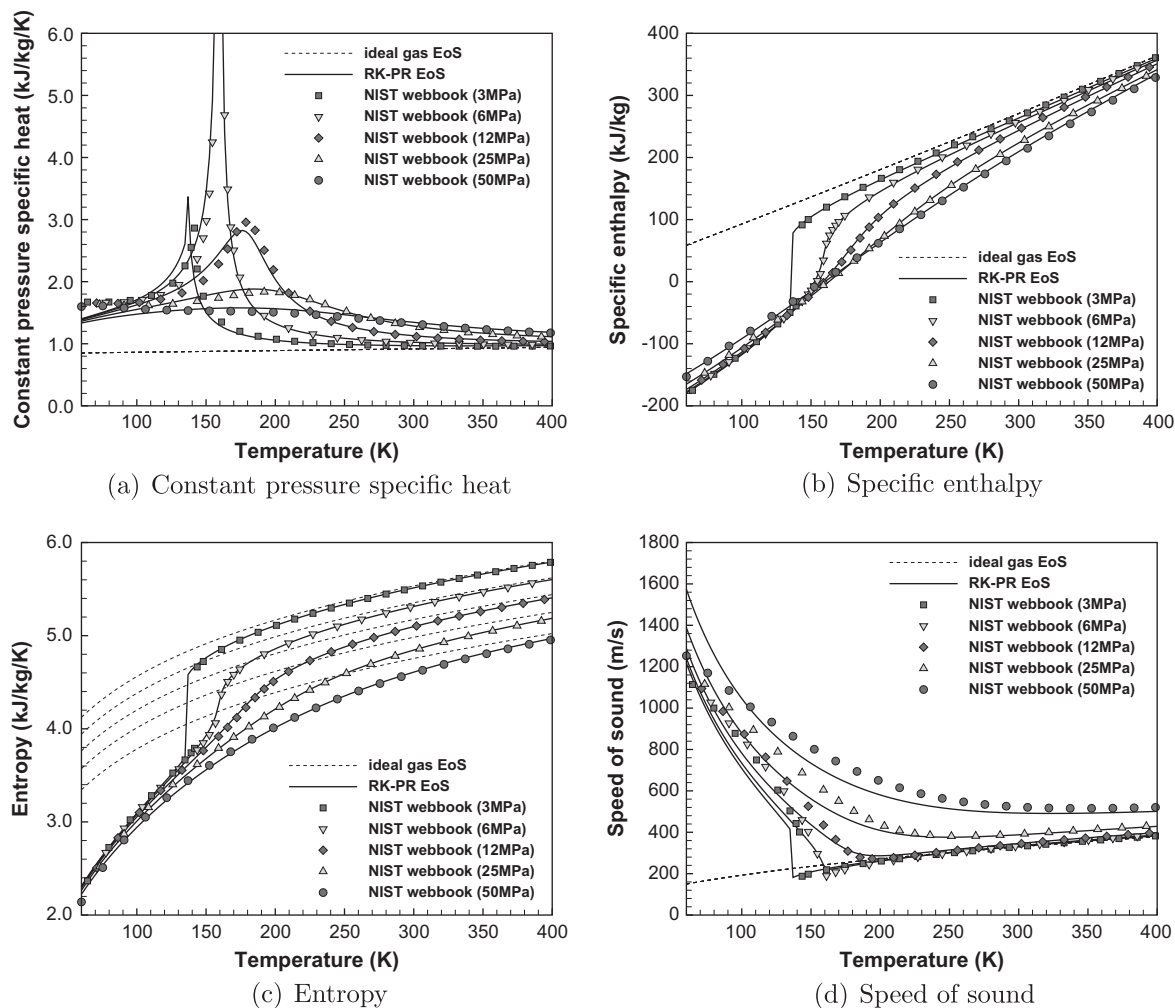


Fig. 4. Thermodynamic properties of oxygen versus temperature for five pressures; comparison between the NIST data (webbook) and the present formulations.

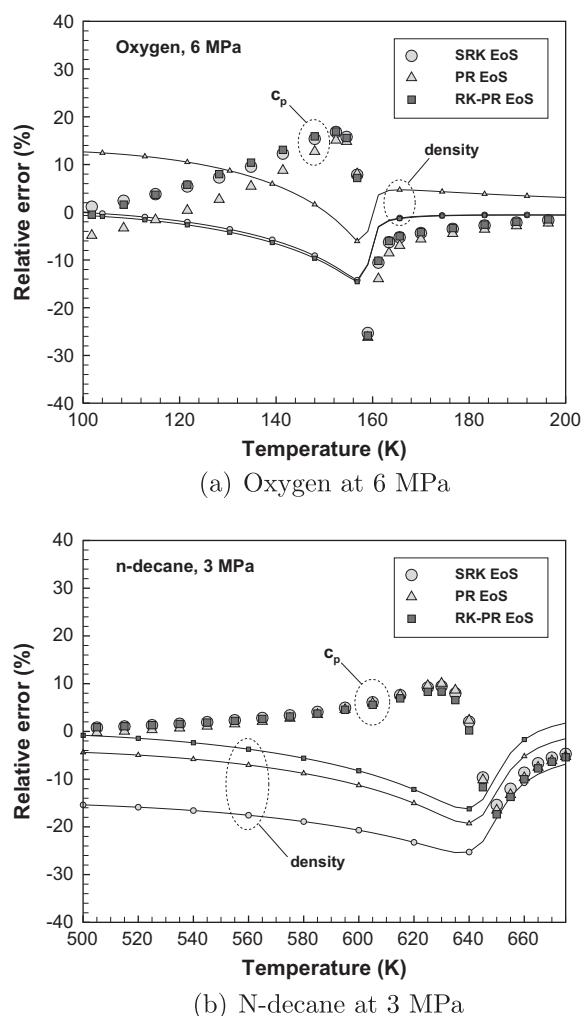


Fig. 5. Relative error of density and constant-pressure specific heat predicted by the three different cubic EoS for oxygen and *n*-decane at near-critical pressures. Reference data is taken from the NIST webbook.

and RK-PR) are compared for oxygen and *n*-decane at the near-critical pressure conditions of 6 MPa and 3 MPa, respectively, in Fig. 5. Similar to the density, the RK-PR EoS provides an identical prediction of the constant-pressure specific heat for oxygen to that of the SRK, whereas the result of the RK-PR is closer to the PR for *n*-decane. This is in line with the results shown in Figs. 1 and 2. The predictive capability of the RK-PR EoS for the constant-pressure specific heat is not noticeably improved compared to *pVT* behavior. It is necessary to note that the thermodynamic properties are derived commonly through the fundamental thermodynamic relations, not only with the generalized cubic equation of state, but also with its derivatives. Consequently, the accuracy of the present thermodynamic model is inevitably governed by the inherent limitation of the cubic equation of state.

Since kerosene fuels, including Jet-A and RP-1, are complex mixtures composed of hundreds of hydrocarbons such as paraffins, naphthenes (cycloparaffins), and aromatics, an approach to model the actual fuel with all of the individual constituents is not feasible. Therefore, there has been a great deal of recent research interest in developing a surrogate mixture model which uses a mixture of a relatively small number of components (usually three to ten) to represent the essential physical or chemical properties of the actual complex fuel [24–28]. Remarkable progress on the chemical kinetic modeling of kerosene surrogates has been made by several collaborative groups [24–26], with a focus on the combustion

behaviors of the actual fuels such as flame speed, ignition delay, and pollutant formation associated mainly with fuel oxidation chemistry. On the other hand, research efforts mainly contributed by NIST are focused on developing surrogate mixture models which realistically represent thermophysical properties such as volatility, density, sound speed, viscosity, thermal conductivity, and cetane number of the jet fuel (Jet-A/JP-8) [27] and rocket fuel (RP-1/RP-2) [28]. The primary goal of this work is to assess the accuracy and applicability of the thermodynamic model derived from the newly developed EoS [15] for the simulation of multi-component reacting flows. However, the issues regarding the physical surrogate models are not discussed because the validity of the surrogate mixture model for calculating the physical properties of the actual kerosene fuel is beyond the scope of this work.

Throughout this study, kerosene fuel is modeled as a surrogate mixture consisting of three components, according to the work of Dagaut and Cathonnet [24,29]. To validate the present thermodynamic model for the kerosene surrogate, reference data is obtained from the NIST Thermophysical Properties of Hydrocarbon Mixtures Database (SUPERTRAPP) [17], which can accurately calculate the properties of more than 200 different hydrocarbon components and their mixtures based on the NIST extended corresponding states model [30]. As will be discussed in subSection 3.3, the flamelet analysis was performed utilizing the detailed chemical kinetics proposed by Dagaut and Cathonnet [24] for a kerosene surrogate with a molar composition of 74% *n*-decane, 11% *n*-propylcyclohexane, and 15% *n*-propylbenzene to represent the different classes of paraffins, cycloalkanes, and aromatics, respectively. However, *n*-propylcyclohexane is not included in the database of SUPERTRAPP. For the purpose of comparison between the present thermodynamic model and SUPERTRAPP, therefore, we utilized an alternative surrogate mixture with a molar composition of 78% *n*-decane, 9.8% cyclohexane, and 12.2% toluene, which was proposed in the previous work of Cathonnet et al. [29].

In terms of the kerosene density profiles versus temperature for five pressures, Fig. 6 presents a comparison between the reference data of SUPERTRAPP and the density profiles predicted by the three different cubic EoS. Contrary to the predicted profiles of oxygen density displayed in Fig. 3, the PR EoS yields closer conformity with SUPERTRAPP, while the SRK EoS considerably underestimates the density level. The RK-PR EoS shows slightly better performance than the PR EoS over the whole temperature and pressure ranges, except for that of the relatively higher temperatures (>500 K) and higher pressures (>25 MPa). For this kerosene surrogate mixture, if we consider that the critical compressibility factors of *n*-decane, cyclohexane, and toluene are 0.2564, 0.2729, and 0.2638, respectively, the predictive trends of the three different EoS are basically consistent with those presented in Figs. 1 and 2.

Figure 7 exhibits a comparison between the SUPERTRAPP data and the thermodynamic properties of the kerosene surrogate mixture predicted by the present model based on the RK-PR EoS. The thermodynamic properties of the kerosene surrogate are qualitatively similar in overall tendency compared with those of oxygen illustrated in Fig. 4 but have quantitatively different characteristics. Compared to cryogenic oxygen ($T_c = 154.6$ K, $p_c = 5.04$ MPa), the kerosene fuel (typically $T_c = 683$ K, $p_c = 2.3$ MPa [1]) exhibits a much higher pseudo-boiling temperature and a much weaker dependency of the thermodynamic properties on pressure and temperature. The present results agree with those of SUPERTRAPP, and the discrepancy between them may be acceptable in engineering calculations.

3.2. Application to the Burke-Schumann flame sheet model

Prior to the flamelet analysis, the present thermodynamic model was applied to a flame sheet with an infinitely fast reaction rate

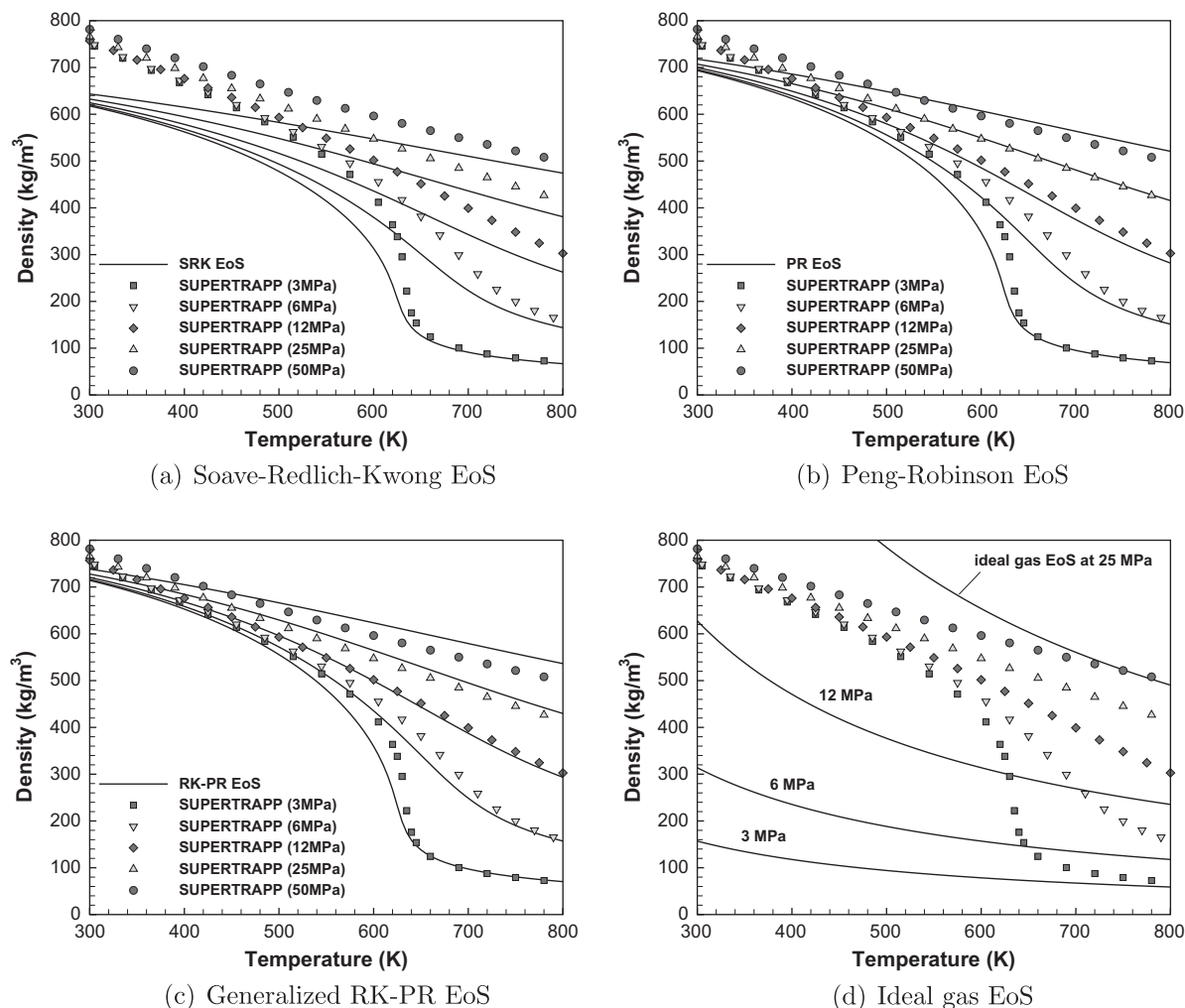
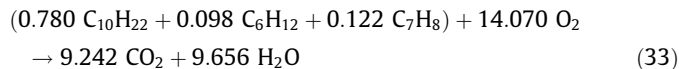


Fig. 6. Density of the kerosene surrogate (78% *n*-decane, 9.8% cyclohexane, and 12.2% toluene by volume) versus temperature for five pressures; comparison between the NIST data (SUPERTRAPP) and predictions by four different EoS.

between the kerosene surrogate and liquid oxygen and was validated against the SUPERTRAPP data. For the same surrogate mixture used in subSection 3.1, the chemistry can be expressed simply by the following one-step global reaction scheme.



Therefore, a mixture within the flame sheet is composed of the six species (*n*-decane, cyclohexane, toluene, oxygen, carbon dioxide, and water vapor) in Eq. (33).

Figure 8 presents a comparison between the SUPERTRAPP results and density profiles predicted by the three different cubic EoS, as well as by the ideal gas assumption for the same temperature and composition which are determined by the Burke-Schumann solution as a function of the mixture fraction. The temperatures of the fuel and oxidizer are 300 K and 100 K, respectively, and the chosen pressure is 6 MPa, corresponding to the typical operating condition for a kerosene/LOx rocket engine with a gas-generator cycle, as listed in Table 1, and the largest variation of oxygen specific heat presented in Fig. 4. Due to the heat and products transported from the flame front by molecular diffusion, rapid changes in density take place near the fuel-rich and oxidizer-rich zones. It is also observed that the oxygen-rich side has a much higher density gradient in the mixture fraction space com-

pared to that on the fuel-rich side. As expected, the SRK EoS correctly predicts the density profile in the vicinity of liquid oxygen but substantially underestimates the density of the kerosene-rich side, whereas the PR EoS predicts the opposite trend. On the other hand, the RK-PR EoS conforms well to the density profile calculated by SUPERTRAPP over the whole mixture fraction space. As the temperature continuously increases by moving toward the stoichiometry in the mixture fraction space, the real fluid effects progressively vanish and all EoS models exhibit ideal gas behavior in the high-temperature regions.

Figure 9 presents the calculated profiles of constant-pressure specific heat and sound speed in the narrow regions close to the oxidizer and fuel sides, respectively. When the mixture states are close to the pseudo-boiling regions for both fuel and oxidizer, the real fluid behavior is dominant though the peak of constant-pressure specific heat. In proximity to the kerosene and liquid oxygen, the real fluid mixtures exhibit a much higher speed of sound than that of the ideal gas assumption. Although the oxygen-rich zone and the fuel-rich zone with the pronounced real fluid effects exist only in limited regions in the mixture fraction space, the corresponding mixing and flame field near the injectors of the kerosene/LOx rocket combustion chamber could be greatly modified by the real fluid effects in terms of density, specific heat, speed of sound, and transport properties. Cutrone et al. [10] have recently reported that the real fluid behavior significantly influenced the

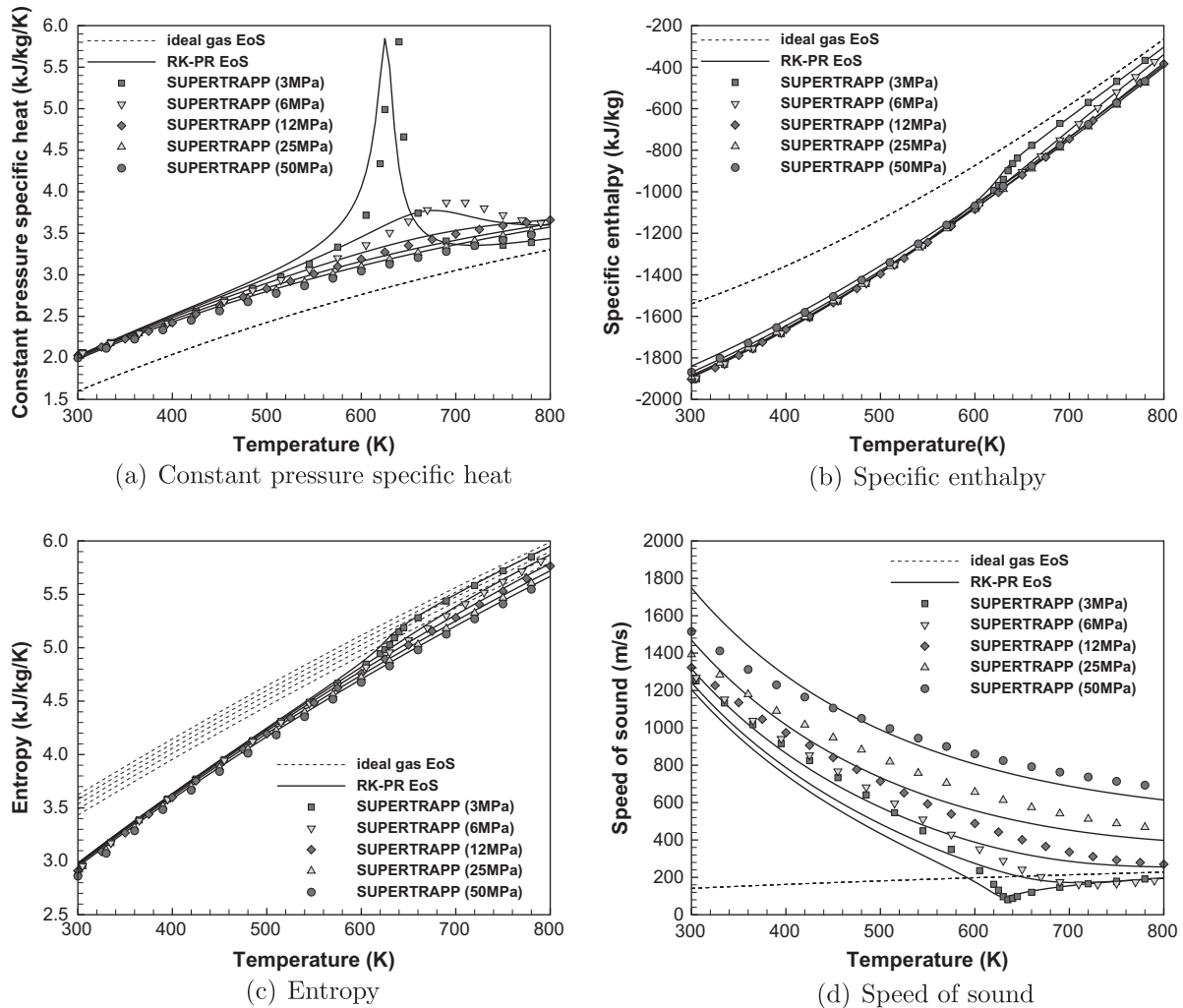


Fig. 7. Thermodynamic properties of the kerosene surrogate versus temperature for five pressures; comparison between the NIST data (SUPERTRAPP) and the present formulations.

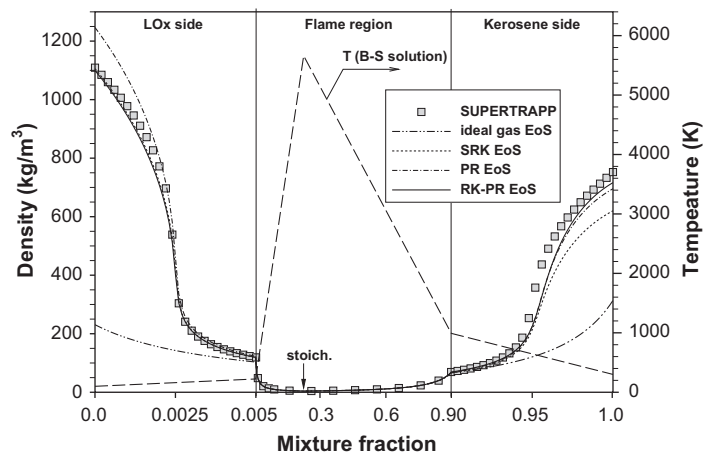


Fig. 8. Comparison of the density profiles calculated by SUPERTRAPP and four different EoS for the Burke-Schumann flame sheet of the kerosene surrogate (300 K) and liquid oxygen (100 K) at 6 MPa.

precise flame structures in a coaxial shear injector of gaseous hydrogen and liquid oxygen at 6 MPa. As shown in Fig. 9, discrepancies exist between the present results and the SUPERTRAPP results, especially for the sound speed of both the dense-fluid

regions and the peak of constant-pressure specific heat in the vicinity of the kerosene side. However, mainly by virtue of the applicability and computational efficiency, the thermodynamic model based on the RK-PR EoS could be widely utilized for the

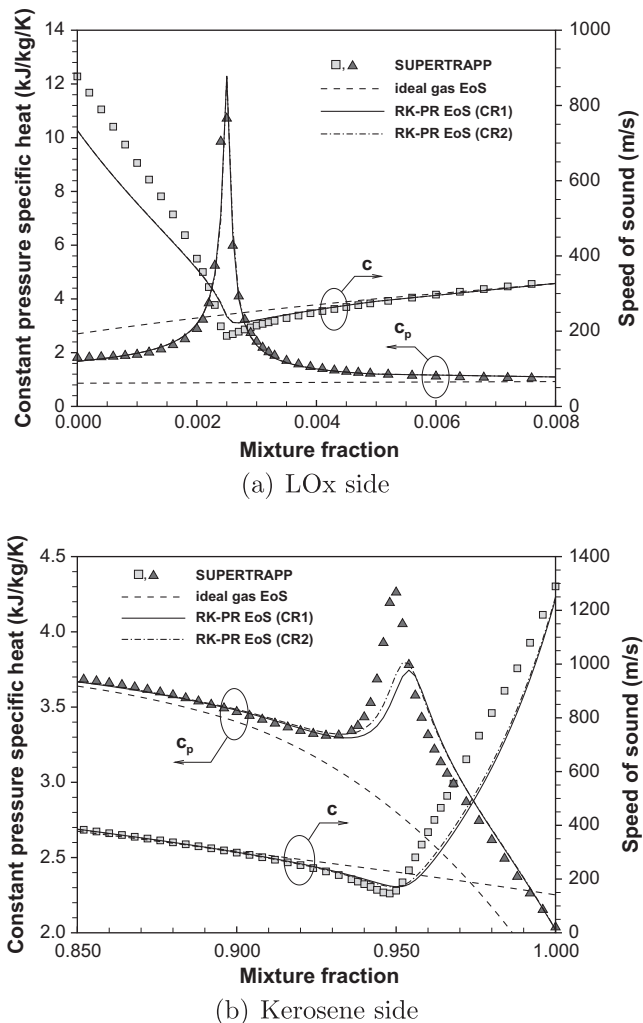


Fig. 9. Comparison of the thermodynamic properties within the oxidizer-rich and fuel-rich regions of the Burke-Schumann flame sheet at 6 MPa.

numerical analysis of various liquid propellant flame fields over the wide range of operating conditions.

Next, we evaluated the effects of the combination rules on the thermodynamic properties based on the numerical results of the Burke-Schumann flame sheet for the kerosene surrogate and liquid oxygen. Numerical results presented in Fig. 9 indicate that the two different combination rules yield nearly identical results in the overall mixture fraction space, except in the very fuel-rich mixing zone, where CR2 predicts slightly higher values than CR1 for the peak of the constant-pressure specific heat. These numerical results suggest that numerical simulation of high pressure mixing and combustion near kerosene/LOx rocket injectors could be marginally influenced by the combination rules.

3.3. Real-fluid based flamelet analysis

In order to model chemical reaction rates in flamelet Eqs. (29) and (31), we employed the detailed chemistry of Dagaut and Cathonnet [24], which is composed of 1673 reversible reactions among 209 species. The present study has adopted their three-component kerosene surrogate with a molar composition of 74% *n*-decane, 15% *n*-propylbenzene, and 11% *n*-propylcyclohexane. According to their work [24], this chemical kinetics model for kerosene/air agrees with the experimental results for the JSR (Jet Stirred Reactor) at 1, 10, and 40 atm, as well as for the ignition delays at 1 and 20 atm.

To the best of our knowledge, the diffusion flames of kerosene and pure oxygen at high pressures have not yet been analyzed in the context of the flamelet approach. To systematically analyze the non-equilibrium effects on the local flame structure of the kerosene surrogate and oxygen, the steady flamelet results under the ideal gas assumption are compared with those of the chemical equilibrium solver (STANJAN [31]). Figure 10 shows that the departures from equilibrium are progressively pronounced at the fuel-rich region, depending on the scalar dissipation rate. Especially for the mixture fractions greater than 0.8, the equilibrium chemistry predicts unrealistic concentrations of CO₂ and CH₄. On the other hand, due to the oxy flame condition at high pressure, the flame temperature near the stoichiometry is higher than 3600 K, and the flame properties of the mixture fraction less than 0.32 remain at the near-equilibrium level for a wide range of scalar dissipation rate, up to $\chi_{st} = 10^4 \text{ s}^{-1}$. As the scalar dissipation rate increases further, the molecular diffusions of mass and heat within the flamelet are predominantly enhanced and lead to a distinctly different flame structure at the near-extinction limit of $\chi_{st} = 9 \times 10^5 \text{ s}^{-1}$.

Subsequently, the real fluid effects on the local flame structures are exhibited in Fig. 11. The steady flamelet solutions based on both the ideal gas and RK-PR EoS are presented in terms of the constant-pressure specific heat and temperature in proximity to the kerosene and oxygen sides. In the oxygen-rich mixture fraction space ($Z < 0.02$) and fuel-rich mixture fraction space ($Z > 0.85$), where real fluid effects play a crucial role, the real-fluid flamelet model yields an abrupt change in the constant-pressure specific heat compared to that of the ideal gas model. In the mixture fraction space, the maximum constant-pressure specific heat corresponds to the pseudo-boiling temperature. In the transcritical mixtures, the location of the peak constant-pressure specific heat is shifted slightly toward the hot flame zone by increasing the scalar dissipation rate. At the steady state, substituting Eq. (29) into Eq. (31) leads to the following relation.

$$\frac{\partial^2 h}{\partial Z^2} = 0 \quad (34)$$

The above equation implies that the dependency of mixture enthalpy on the mixture fraction is a linear function with the two boundary values at the fuel and oxidizer, regardless of chemical reactions and the scalar dissipation rate under the unitary Lewis numbers, adiabatic, and steady state assumptions. In these regions where the real fluid mixture undergoes transcritical transition at the pseudo-boiling points, the heat diffused from the flame front is consumed to rapidly expand the volume rather than to increase the temperature. The ideal-gas flamelet model predicts the quasi-linear profiles of temperature due to the smooth variation in constant-pressure specific heat, while the real-fluid flamelet model yields a temperature plateau near the peak of the constant-pressure specific heat. Accordingly, the real-fluid flamelet model predicts a relatively lower temperature distribution compared to that of the ideal-gas flamelet model. As shown in Fig. 11(a), nine grid points are clustered in a very narrow region ($0 < Z < 0.02$) to demonstrate the peak movement of the constant-pressure specific heat with a varying scalar dissipation rate. Actually, grid independence for the steady flamelet solution is achieved even with coarser grids in this mixture region because we use the flamelet energy Eq. (31) in terms of the second derivative of mixture enthalpy. In the mixture region very close to the oxidizer, the reaction rates are negligibly small, and the species and heat are transported only by the molecular diffusion between the oxidizer and the flame zones, as shown in Fig. 12. With the convergence of the solutions to the flamelet equations (Eqs. (29) and (31)), the second derivatives of the mass fractions and

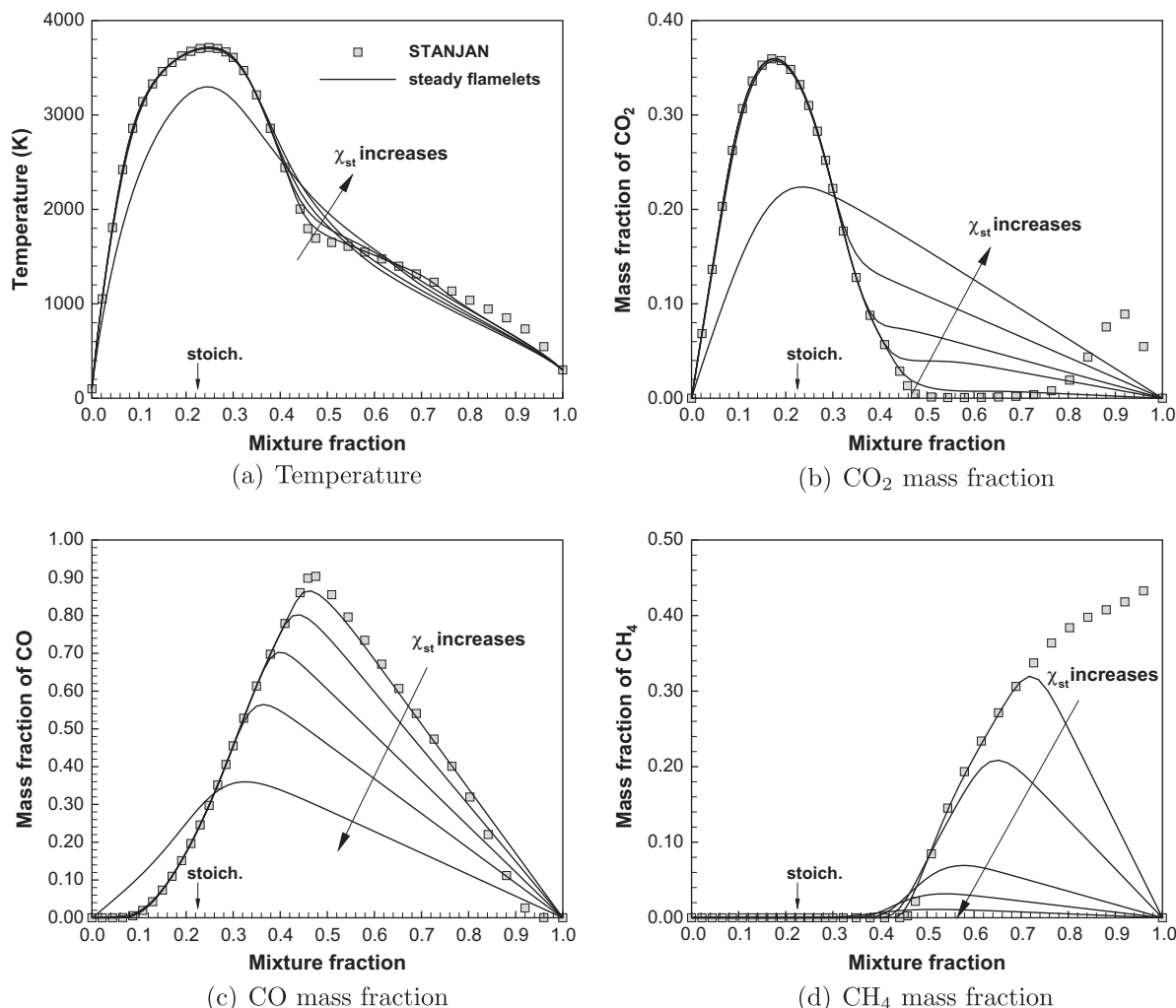


Fig. 10. Non-equilibrium effects on flame structures of the kerosene surrogate (74% *n*-decane, 15% *n*-propylbenzene, and 11% *n*-propylcyclohexane by volume) and oxygen at 6 MPa; symbols: chemical equilibrium (STANJAN); solid lines: steady flamelet solutions (ideal gas) at $\chi_{st} = 10^{-2}, 1, 10^2, 10^4$, and $9 \times 10^5 \text{ s}^{-1}$.

mixture enthalpy with respect to the mixture fraction are nearly zero in the mixing region, and the steady state solutions are not affected by the grid refinement in the region ($0 < Z < 0.02$). If the conventional energy equation of Eq. (30) was used instead, with derivatives of temperature and constant-pressure specific heat, much more grid points in the mixing region with pseudo-boiling would be needed to achieve grid independence for the real-fluid flamelet solutions.

Figure 12 shows the detailed flame structure of the kerosene surrogate and liquid oxygen predicted by steady flamelet analysis based on the ideal gas assumption and the RK-PR EoS. Since the mixture in the high temperature region behaves like an ideal gas, the two flamelet models yield nearly identical distributions for temperature and species mass fractions within the flamelet, except for those in the immediate vicinities of the oxygen and kerosene sides. The distribution of the heat release rate given in Fig. 12b shows that there are two endothermic peaks and two exothermic peaks in the fuel-rich and oxidizer-rich regions, respectively. Similarly, Pons et al. [8] identified one endothermic peak corresponding to the methane pyrolysis and two peaks related to exothermic oxidation reactions in the numerical result of the counterflow diffusion flame for methane/oxygen. In the present results, the first peak close to the fuel side is associated with the pyrolysis of the main constituents of the kerosene surrogate, while

the next peak reflects a further breakdown of the smaller hydrocarbons like methane to hydrogen and carbon monoxide. The first and second peaks in the oxidizer-rich region correspond to the main products of combustion, CO_2 and H_2O , respectively.

Next, we numerically investigated the effects of elevating pressure on the flame structures. For comparative purposes, the ideal-gas flamelet calculation was also performed for the flame structure between the kerosene surrogate and air at a pressure of 6 MPa and a propellant temperature of 300 K. When air was used as the oxidizer, the maximum temperature at the low value of the scalar dissipation rate ($\chi_{st} = 10^{-2} \text{ s}^{-1}$) was 2356 K, and flame extinction occurred at $\chi_{st} = 3.9 \times 10^2 \text{ s}^{-1}$. On the other hand, as shown in Fig. 13, the kerosene flames with pure oxygen possess a much higher flame temperature, and the extinction limit elongates greatly to a value of χ_{st} higher than $7 \times 10^5 \text{ s}^{-1}$ at the same condition. Numerical results also indicate that the real fluid effects decrease the flame temperature by approximately 40 K over the pressure conditions of interest, as discussed in Figs. 11 and 12(a). By elevating the pressure, the flame temperature increases due to the reduction of chemical dissociation, and the extinction limit is extended. Mainly due to the unique combustion characteristics associated with the high-pressure oxy flame, it is expected that the flame field at the near-injector region will be substantially resistant to the extinction induced by turbulent

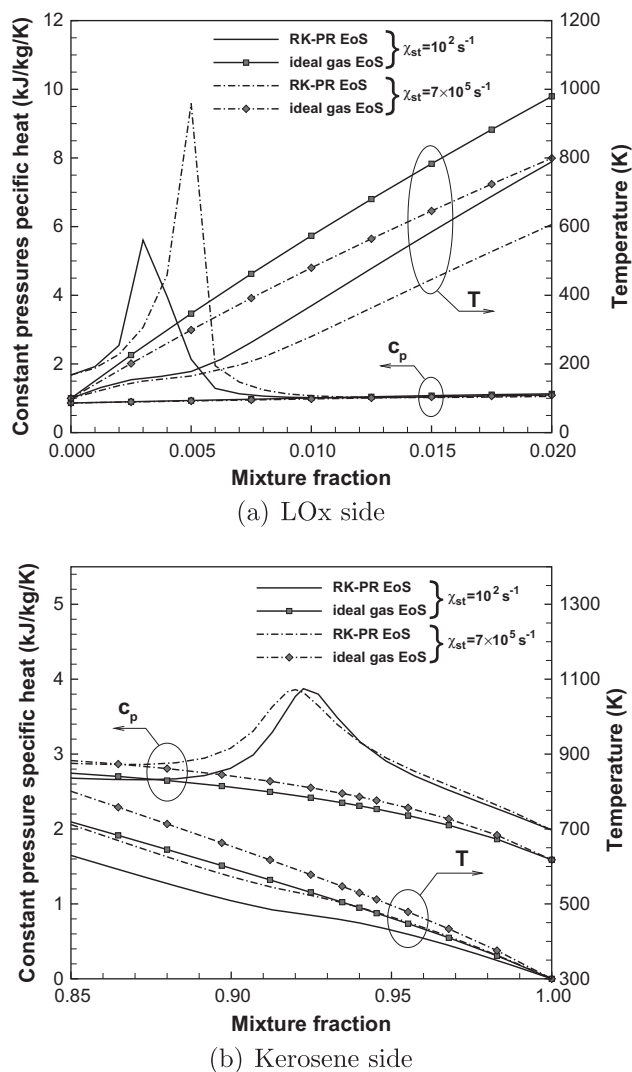


Fig. 11. Steady flamelet solutions near the kerosene surrogate (300 K) and liquid oxygen (100 K) at 6 MPa.

mixing within the actual combustion chambers of liquid rocket engines.

Figure 14 clearly shows that the maximum heat release rate of the flamelet is logarithmically correlated with the product of the scalar dissipation rate and pressure. The linear dependency of the heat release rate on the scalar dissipation rate or the strain rate at supercritical pressures is consistently in line with those of the previous results of the counterflow diffusion flames for hydrogen/oxygen [6] and methane/oxygen [8], as well as the flamelet calculation for hydrogen/oxygen [32].

4. Conclusion

This study developed a thermodynamic model based on the newly developed three-parameter cubic EoS for the simulation of multi-component reacting flows at supercritical pressure conditions. The numerical results clearly indicate that the present model is superior to those of the SRK and PR EoS in handling the fluid mixtures with different critical compressibility factors over a wide pressure and temperature range. Moreover, in the framework of the real-fluid flamelet formulation, the present study investigated the local flame structures of kerosene and liquid oxygen in super-

critical pressure conditions encountered in the liquid propellant rocket engine.

- The three-parameter cubic equation of state (RK-PR EoS) recently proposed by Cismondi and Mollerup [15] has demonstrated superior accuracy in predicting pVT behaviors of individual fluids and mixtures having quite different critical compressibility factors (Z_c) over a wide pressure and temperature range compared to those of the two-parameter cubic EoS, such as the Soave–Redlich–Kwong (SRK) and Peng–Robinson (PR) models.
- In this study, in order to apply the RK-PR EoS to the simulation of the multi-component reacting mixture, the thermodynamic properties were fully derived from the fundamental thermodynamic relations and the conventional mixing rule. Compared to the NIST database based on the extended corresponding states model, the present thermodynamic model is able to correctly predict the thermodynamic non-idealities near the dense-fluid regions for both cryogenic oxygen and the three-component kerosene surrogate. In terms of the numerical modeling, the generalized formulations in this study can also be straightforwardly incorporated to simulation frameworks developed previously based on the two-parameter cubic EoS; for example, the preconditioning scheme based on the SRK EoS [7].
- In comparison with the NIST SURPERTRAPP results for the Burke–Schumann flame sheet of the kerosene surrogate and liquid oxygen, the SRK EoS correctly predicts the density profile in the vicinity of liquid oxygen but substantially underestimates the density level on the kerosene-rich side, whereas the PR EoS predicts the opposite trend. On the other hand, the RK-PR EoS conforms well to the density profile calculated by SUPERTRAPP over the whole mixture fraction space. Discrepancies exist between the present results and the SUPERTRAPP data, especially for the sound speed for the dense-fluid regions and the peak value of the constant-pressure specific heat on the kerosene side. Mainly by virtue of the applicability and computational efficiency, however, the thermodynamic model based on the RK-PR EoS could be widely utilized for numerically analyzing various liquid propellant flame fields over a wide range of operating conditions.
- Numerical results indicate that the two different combination rules yield nearly identical results in the overall mixture fraction space, except for the very fuel-rich mixing zone where CR2 predicts slightly higher values than CR1 for the peak of the constant-pressure specific heat. These numerical results suggest that numerical simulation of high pressure mixing and combustion near kerosene/LOx rocket injectors could be marginally influenced by the combination rules.
- Steady flamelet analysis based on the present thermodynamic modeling was performed in order to investigate the effects of detailed chemical kinetics, real fluid behavior, and elevating pressures on the local flame structures of the kerosene surrogate and cryogenic liquid oxygen at high pressures relevant to existing kerosene-fueled rocket engines. It is expected that the present real-fluid flamelet equations could be useful for simulating a turbulent kerosene/LOx flame field in actual liquid rocket combustion chambers because of its predictive capability to simultaneously take into account the non-equilibrium effects pronounced in the hydrocarbon-fuel rich region and the dense-fluid behaviors due to the transcritical transition of liquid propellants in the near-injector region.
- The different chemical kinetics along with the kerosene surrogate models need to be assessed with a focus on validity of the high pressure conditions with pure oxygen, and the result will be relevant to actual liquid rocket engines. In our future

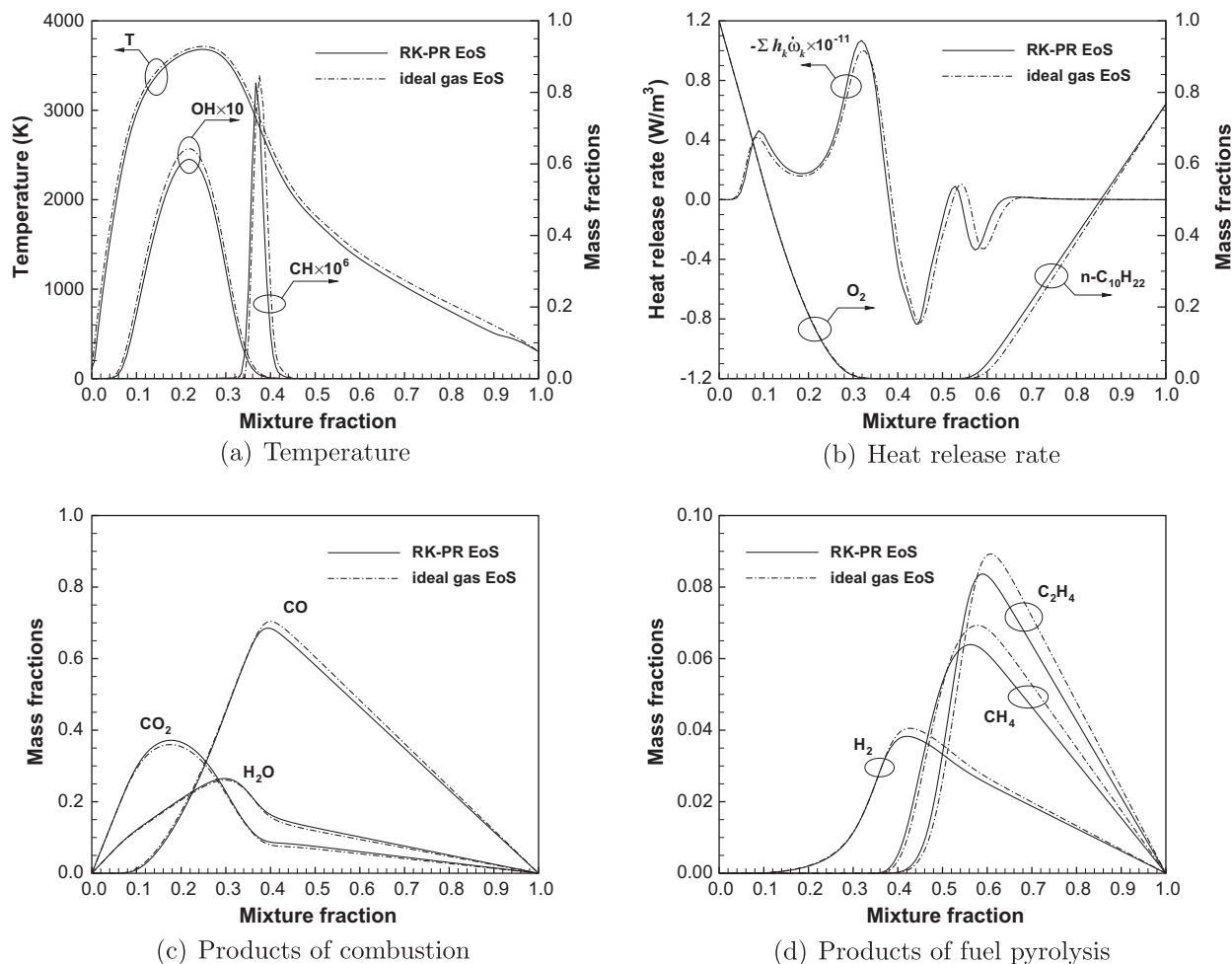


Fig. 12. Flame structures of the kerosene surrogate and liquid oxygen at 6 MPa and $\chi_{st} = 10^2 \text{ s}^{-1}$.

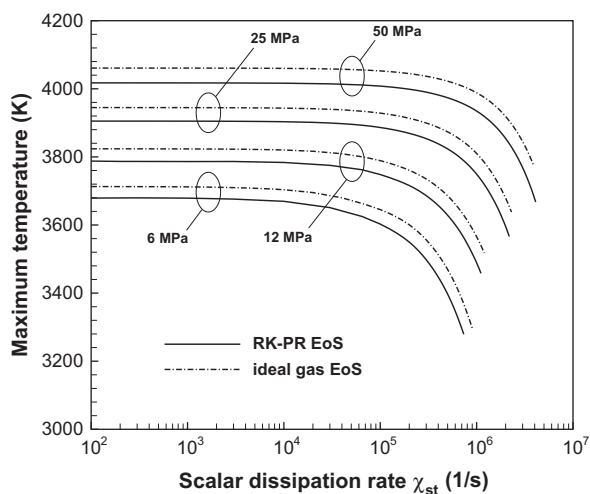


Fig. 13. Effect of scalar dissipation rate on the maximum temperature of the steady flamelets of the kerosene surrogate and liquid oxygen at different pressures.

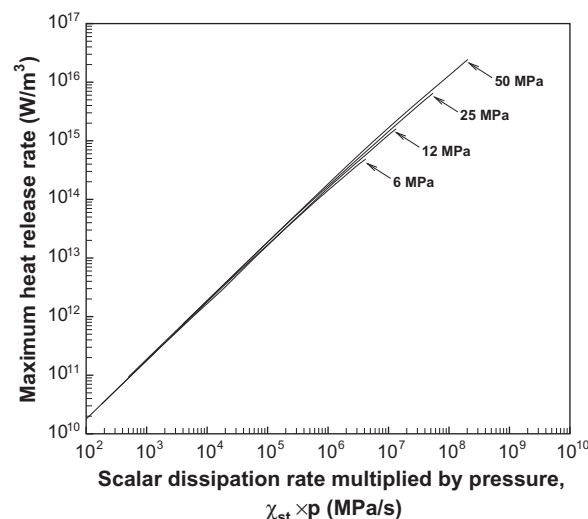


Fig. 14. Maximum heat release rate correlated with the product of scalar dissipation rate and pressure from the steady flamelet solutions with the RK-PR EoS.

work, the issues related to the effects of differential diffusion and radiative loss on the stationary flame structures and the interaction between transient flamelets and pressure oscillations will be systematically investigated.

Acknowledgments

The authors thank Dr. Philippe Dagaut of CNRS for providing the detailed chemical kinetic mechanism and additional information.

The present work was carried out under the Research and Development of the Korea Space Launch Vehicle-II project sponsored by the Ministry of Education, Science and Technology. It was partially supported by the National Space Lab program through the National Research Foundation of Korea (No. 20090091793).

References

- [1] T. Edwards, J. Propul. Power 19 (6) (2003) 1089–1107.
- [2] G.P. Sutton, History of Liquid Propellant Rocket Engines, AIAA, Reston, VA, 2005.
- [3] J. Bellan, Prog. Energy Combust. Sci. 26 (2000) 329–366.
- [4] V. Yang, Proc. Combust. Inst. 28 (2000) 925–942.
- [5] J.C. Oefelein, V. Yang (Eds.), Combustion Science and Technology Special Issue: Supercritical Fluid Transport and Combustion, Combust. Sci. Technol. 178 (1–3) (2006) 1–621.
- [6] G. Ribert, N. Zong, V. Yang, L. Pons, N. Darabiha, S. Candel, Combust. Flame 154 (2008) 319–330.
- [7] H. Meng, V. Yang, J. Comput. Phys. 189 (2003) 277–304.
- [8] L. Pons, N. Darabiha, S. Candel, G. Ribert, V. Yang, Combust. Theory Model. 13 (2009) 57–81.
- [9] N. Zong, G. Ribert, V. Yang, AIAA Paper No. 2008-946, 2008.
- [10] L. Cutrone, P. De Palma, G. Pascazio, M. Napolitano, Comput. Fluids 39 (2010) 485–498.
- [11] R.S. Miller, K.G. Harstad, J. Bellan, J. Fluid Mech. 436 (2001) 1–39.
- [12] M.S. Graboski, T.E. Daubert, Ind. Eng. Chem. Proc. Des. Dev. 17 (1978) 443–448.
- [13] D. Peng, D. Robinson, Ind. Eng. Chem. Fundam. 15 (1976) 59–64.
- [14] R.C. Reid, J.M. Prausnitz, B.E. Poling, The Properties of Gases & Liquids, fourth ed., McGraw-Hill, New York, NY, 1987.
- [15] M. Cismonti, J. Mollerup, Fluid Phase Equilib. 232 (2005) 74–89.
- [16] National Institute of Standards and Technology Webbook, <<http://webbook.nist.gov/chemistry/fluid/>>.
- [17] M.L. Huber, NIST Thermophysical Properties of Hydrocarbon Mixtures Database (SUPERTRAPP), Version 3.1 User's Guide, US Department of Commerce, Gaithersburg, MD, 2003.
- [18] H. Meng, G.C. Hsiao, V. Yang, J.S. Shuen, J. Fluid Mech. 527 (2005) 115–139.
- [19] N. Zong, V. Yang, Phys. Fluids 20 (2008) 1–14.
- [20] R.J. Kee, F.M. Rupley, J.A. Miller, Chemkin II: A FORTRAN chemical kinetics package for analysis of gas phase chemical kinetics, Technical Report SAND89-8009B, Sandia National Laboratories, 1993.
- [21] N. Peters, Turbulent Combustion, Cambridge Univ. Press, Cambridge, UK, 2000.
- [22] S.-K. Kim, S.M. Kang, Y.M. Kim, Combust. Sci. Technol. 168 (2001) 47–83.
- [23] J.F. Grcar, The Twopnt Program for Boundary Value Problems, Technical Report SAND91-8320, Sandia National Laboratories, 1992.
- [24] P. Dagaut, M. Cathonnet, Prog. Energy Combust. Sci. 32 (2006) 48–92.
- [25] S. Dooley, S.H. Won, M. Chaos, J. Heyne, Y. Ju, F.L. Dryer, K. Kumar, C.-J. Sung, H. Wang, M.A. Oehlschlaeger, R.J. Santoro, T.A. Litzinger, Combust. Flame 157 (2010) 2333–2339.
- [26] H. Wang, E. Dames, B. Sirjean, D.A. Sheen, R. Tangko, A. Violi, J.Y.W. Lai, F.N. Egolfopoulos, D.F. Davidson, R.K. Hanson, C.T. Bowman, C.K. Law, W. Tsang, N.P. Cernansky, D.L. Miller, R.P. Lindstedt, A high-temperature chemical kinetic model of *n*-alkane (up to *n*-dodecane), cyclohexane, and methyl-, ethyl-, *n*-propyl and *n*-butyl-cyclohexane oxidation at high temperatures, JetSurF version 2.0, September 19, 2010 <<http://www.melchior.usc.edu/JetSurF/JetSurF2.0>>.
- [27] M.L. Huber, E.W. Lemmon, T.J. Bruno, Energy Fuels 24 (2010) 3565–3571.
- [28] M.L. Huber, E.W. Lemmon, L.S. Ott, T.J. Bruno, Energy Fuels 23 (2009) 3083–3088.
- [29] M. Cathonnet, D. Voisin, A. Etsouli, C. Sferdean, M. Reuillon, J.C. Boettner, P. Dagaut, Res. Technol. Org. Meet. Proc. 14 (1999) 14.
- [30] M.L. Huber, H.J.M. Hanley, The corresponding-states principle: dense fluids, in: J. Millat, J.H. Dymond, C.A. Nieto de Castro (Eds.), Transport Properties of Fluids, Cambridge University Press, 1996 (Chapter 12).
- [31] A.E. Lutz, F.M. Rupley, R.J. Kee, W.C. Reynolds, EQUIL: A CHEMKIN Implementation of STANJAN for Computing Chemical Equilibria, Sandia National Laboratories, 1996.
- [32] T. Kim, Y. Kim, S.-K. Kim, Int. J. Hydrogen Energy 36 (2011) 6303–6316.